

Flatbands and Emergent Ferromagnetic Ordering in Fe_3Sn_2 Kagome LatticesZhiyong Lin,^{1,2} Jin-Ho Choi,³ Qiang Zhang,^{1,2} Wei Qin,¹ Seho Yi,³ Pengdong Wang,⁴ Lin Li,^{1,2} Yifan Wang,^{1,2} Hui Zhang,^{1,2} Zhe Sun,⁴ Laiming Wei,^{1,2} Shengbai Zhang,^{1,5} Tengfei Guo,^{1,6,7} Qingyou Lu,^{1,6,7}Jun-Hyung Cho,^{1,3,†} Changgan Zeng,^{1,2,*} and Zhenyu Zhang¹¹*International Center for Quantum Design of Functional Materials (ICQD), Hefei National Laboratory for Physical Sciences at the Microscale, and Synergetic Innovation Center of Quantum Information and Quantum Physics,**University of Science and Technology of China, Hefei, Anhui 230026, China*²*CAS Key Laboratory of Strongly-Coupled Quantum Matter Physics, and Department of Physics, University of Science and Technology of China, Hefei, Anhui 230026, China*³*Department of Physics and HYU-HPSTAR-CIS High Pressure Research Center, Hanyang University, 17 Haengdang-Dong, SeongDong-Ku, Seoul 133-791, Korea*⁴*National Synchrotron Radiation Laboratory, University of Science and Technology of China, Hefei, Anhui 230029, China*⁵*Department of Physics, Applied Physics and Astronomy, Rensselaer Polytechnic Institute, Troy, New York 12180, USA*⁶*Anhui Key Laboratory of Condensed Matter Physics at Extreme Conditions, High Magnetic Field Laboratory and Hefei Science Center, Chinese Academy of Sciences, Hefei 230031, China*⁷*Collaborative Innovation Center of Advanced Microstructures, Nanjing University, Nanjing 210093, China*

(Received 18 March 2018; revised manuscript received 3 June 2018; published 27 August 2018)

A flatband representing a highly degenerate and dispersionless manifold state of electrons may offer unique opportunities for the emergence of exotic quantum phases. To date, definitive experimental demonstrations of flatbands remain to be accomplished in realistic materials. Here, we present the first experimental observation of a striking flatband near the Fermi level in the layered Fe_3Sn_2 crystal consisting of two Fe kagome lattices separated by a Sn spacing layer. The band flatness is attributed to the local destructive interferences of Bloch wave functions within the kagome lattices, as confirmed through theoretical calculations and modelings. We also establish high-temperature ferromagnetic ordering in the system and interpret the observed collective phenomenon as a consequence of the synergetic effect of electron correlation and the peculiar lattice geometry. Specifically, local spin moments formed by intramolecular exchange interaction are ferromagnetically coupled through a unique network of the hexagonal units in the kagome lattice. Our findings have important implications to exploit emergent flatband physics in special lattice geometries.

DOI: [10.1103/PhysRevLett.121.096401](https://doi.org/10.1103/PhysRevLett.121.096401)

In electronic band theory, the band structures of solids are determined by solving the one-electron Schrödinger equation for electrons in the periodic potential of the lattice [1]. The creation of various nontrivial band structures has been exploited by proper design of the lattice structures. For example, Dirac bands with linear dispersion are realized in the honeycomb lattice [2–4]. Contrasting with this linear Dirac band hosting massless quasiparticles, the dispersionless flatbands render electrons superheavy due to their localization [5–8]. In such flatbands, the kinetic energy of electrons is very quenched, while their mutual Coulomb repulsions prevail. Because of their intriguing electronic features, flatbands have been exploited to develop various emergent effects, including ferromagnetism [5–8], high-temperature fractional quantum Hall effect [9–12], Wigner crystallization [13], Bose-Einstein condensation [14], and high-temperature superconductivity [15,16].

In principle, flatbands can be constructed by a delicate design of the lattice geometry that produces the destructive interference of Bloch wave functions [5–20]. Specifically,

several lattice geometries have been proposed to generate flatbands [5–20], such as the kagome [5–7], side-centered square [8], and checkerboard [10] lattices. In the kagome lattice composed of interlaced triangles where each lattice point interconnects two neighboring hexagons, self-localization of the electron wave functions can be realized by the destructive interference around each hexagon [19], as depicted in Fig. 1(a), thereby leading to a dispersionless flatband. So far, despite many predicted intriguing physical aspects of such lattice-induced flatbands [5–20], flatbands have only been observed in artificially engineered systems such as assemblies of judiciously placed atoms on a two-dimensional (2D) surface and cold atomic systems [21–23]. The experimental observations of flatbands and their exotic electronic properties are still challenging in natural solid state materials. In the present Letter, we demonstrate how flatbands and ferromagnetism can be naturally materialized in a realistic layered 2D kagome compound, Fe_3Sn_2 .

As shown in Figs. 1(b) and 1(c), the structure of Fe_3Sn_2 is composed of two Fe-Sn layers separated by a Sn spacing

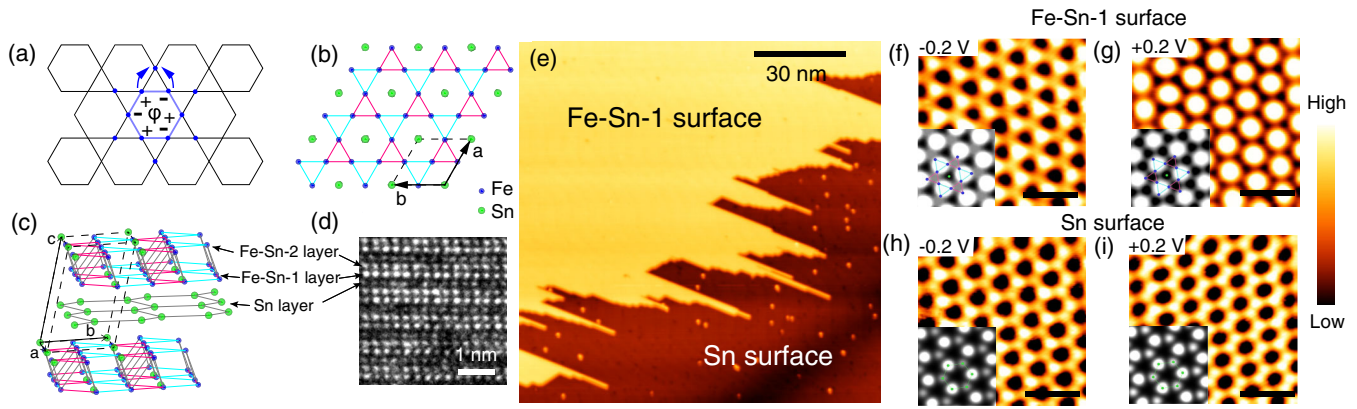


FIG. 1. Structural characterization of the Fe_3Sn_2 bulk and surface. (a) Schematic diagram of the wave function self-localization on the hexagons in the kagome lattice: Because of the special structure of the kagome lattice, the wave function alternates its sign around the six vertices in each hexagon, leading to destructive interference outside of the hexagon and, therefore, electrons locally circulate around each hexagon. (b),(c) Top and perspective views of the optimized structure of bulk Fe_3Sn_2 . The bond lengths in the red and cyan colored triangles are 2.54 and 2.77 Å, respectively. Three different layers are denoted as Fe-Sn-1, Fe-Sn-2, and Sn, respectively. (d) Cross-sectional TEM image with the atomic resolution of three different layers. (e) Large-scale STM image of a cleaved Fe_3Sn_2 surface with two different surface layers. The sample bias was $V_s = 0.4$ V. (f)–(i) Atomic resolution STM images taken at $V_s = 0.2$ and -0.2 V on the two different surface layers. The scale bars in (f)–(i) are 1 nm. The corresponding simulated STM images for the two surface layers are also given in the insets.

layer, where the Fe atoms in each Fe-Sn layer form a kagome lattice [24]. The grown Fe_3Sn_2 single crystal shows a hexagonal shape, whose lateral size amounts to about 3 mm: The x-ray diffraction pattern (Fig. S1 in the Supplemental Material [25]) [24] and cross-sectional transmission electron microscopy (TEM) image [Fig. 1(d)] validate the high crystalline quality and also reveal that the sample surface is parallel to the Fe-Sn layers.

Because of the layered structure of Fe_3Sn_2 , there are three possible terminations at the surface [see Fig. 1(c)]: the Sn layer, the first Fe-Sn layer (hereafter denoted as Fe-Sn-1 layer), and the second Fe-Sn layer (Fe-Sn-2 layer). Figure 1(e) and Fig. S2(a) in the Supplemental Material [25] show the large-scale scanning tunneling microscopy (STM) images, while Fig. S2(b) in the Supplemental Material [25] displays the STM height profile, clearly demonstrating that the cleaved surface is composed of two different surface layers. In order to distinguish the structures of the two observed surface layers, we obtained enlarged STM images at sample biases (V_s) of -0.2 and 0.2 V [see Figs. 1(f)–1(i)]. It is found that the STM images [Figs. 1(f) and 1(g)] for the upper surface layer show bias-dependent features: i.e., buckled honeycomb pattern and hexagonally close-packed bright spots at -0.2 and 0.2 V, respectively. Meanwhile, the STM images for the lower surface layer [Figs. 1(h) and 1(i)] show a similar honeycomb pattern at both biases.

It is noted that the STM images mainly reflect the spatial variation of the local density of states (LDOS) at the surface instead of a direct imaging of the surface atomic structure [33]. Therefore, it is usually difficult to determine the surface structure only from the experimental STM images, especially when the spatial distribution of the LDOS

deviates from the atomic structure. In such cases, the combination of the experimental STM images and simulated ones is a powerful approach and has been widely adopted to identify the surface structures [34]. Therefore, to identify the two observed surface layers, we simulated the STM images of all three possible surface structures using the Tersoff-Hamann approximation [35,36] (see more details in the “First-principles calculations” section of the Supplemental Material [25]). The results for the Fe-Sn-1 and Sn structures are displayed in the insets of Figs. 1(f)–1(i), while that for the Fe-Sn-2 structure in Fig. S3 in the Supplemental Material [25]. For the Fe-Sn-1 surface, the simulated filled- and empty-state STM images show a strongly buckled honeycomb pattern and hexagonally close-packed bright protrusions, respectively, arising from the two types of Fe triangles with different Fe-Fe bond lengths [see Fig. 1(b)]. On the other hand, for the Sn surface, the simulated filled- and empty-state STM images show a honeycomb pattern with three bright and three less-bright protrusions representing a buckled honeycomb lattice of Sn. Here, the height difference between the buckled surface Sn atoms is calculated to be 0.152 Å. These features of the simulated STM images of the Fe-Sn-1 and Sn surface structures agree well with those of the experimental images [see Figs. 1(f)–1(i)]. Therefore, we conclude that the two observed surface layers are the Fe-Sn-1 and Sn layers. It is noted that the simulated STM images of the Fe-Sn-2 surface have similar patterns as those of Fe-Sn-1. However, the STM height-profile measurement at 0.2 V shows that the layers with hexagonally close-packed bright spots are positioned at ~ 2 Å higher or ~ 4 Å lower than the other layer with the honeycomb pattern [see Fig. S2(b) in the Supplemental Material [25]]. This result

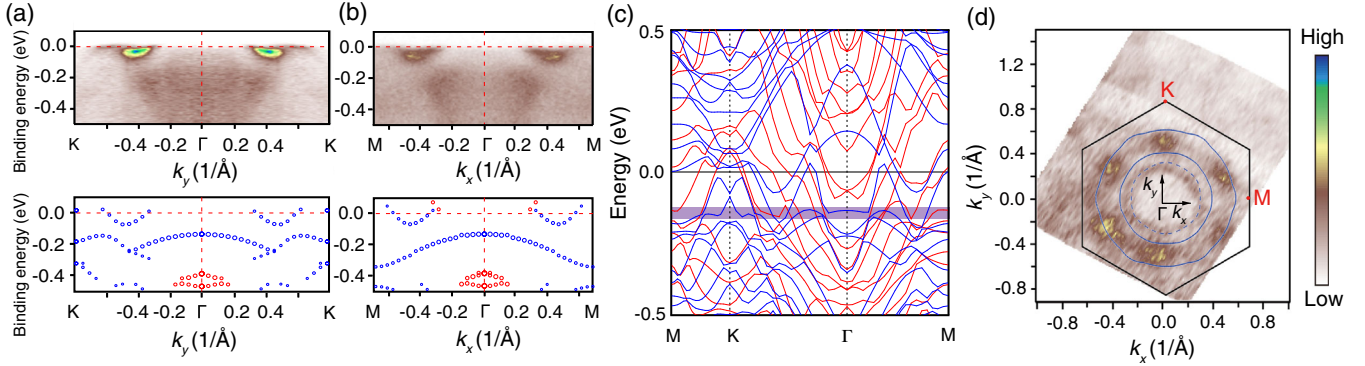


FIG. 2. Electronic band structure of the Fe_3Sn_2 surface. (a),(b) (Top) ARPES results along the Γ - K and Γ - M lines, respectively. (Bottom) Calculated spin-polarized bands projected onto the top few layers of the Fe-Sn-1 surface structure. Here, the majority (minority) spin bands are drawn with the red (blue) circles whose sizes are proportional to the weights of the projected electrons. (c) Calculated spin-polarized band structure for the Fe-Sn-1 surface structure. Here, the Fermi level E_F is set at zero energy, and the purple shaded stripe highlights the nearly flatbands close to -0.2 eV. (d) Photoemission intensity map at the Fermi level superimposed with the calculated Fermi surfaces for the Fe-Sn-1 (solid circles) and Sn (dashed circle) surfaces.

unambiguously indicates that the former layer is Fe-Sn-1, rather than Fe-Sn-2. Moreover, density-functional theory (DFT) total-energy calculations demonstrate that the order of the thermodynamic stability is $\text{Sn} > \text{Fe-Sn-1} > \text{Fe-Sn-2}$ over a wide range of the Sn chemical potential (see Fig. S4 and more discussions in the Supplemental Material [25]), consistent with the experimental observations of Sn and Fe-Sn-1. It is most likely that the Fe-Sn-2 surface layer decomposes during or very shortly after the cleaving process because the cleavage temperature of about 80 K is not low enough to prevent the lattice relaxation. Indeed, high-density bright spots are clearly observed on the Sn surface [see Fig. 1(e) and Fig. S2(a) in the Supplemental Material [25]], which could be the residues of the Fe-Sn-2 decomposition.

Next, we measured the low-energy electronic structure of the Fe_3Sn_2 surface by angle-resolved photoemission spectroscopy (ARPES). Strikingly, the ARPES data along the Γ - K and Γ - M lines reveal a nearly dispersionless flatband at ~ 0.2 eV below E_F [see Figs. 2(a) and 2(b)]. The presence of such a flatband can be more apparently seen in the second derivative ARPES data (see Fig. S5 in the Supplemental Material [25]). Here, the flat dispersion extends more than half of the Γ - K and Γ - M lines. To quantitatively understand the observed flatband, we calculated the band structures for the bulk, Fe-Sn-1, and Sn surface structures. Their spin-polarized band structures are displayed in Fig. S6 in the Supplemental Material [25] and Fig. 2(c), respectively, showing partially flat dispersions of some bands around ~ 0.2 eV below E_F .

Since the ARPES measurement with photon energy of 35 eV is highly surface sensitive, we projected the calculated bands onto the atoms near the surface up to the third subsurface layers to compare with the ARPES data. As shown in Figs. 2(a) and 2(b), the bands localized near the Fe-Sn-1 surface are in reasonably good agreement with the ARPES data. In particular, there exist narrow

bands at ~ 0.2 eV below E_F as well as the electron pockets along the Γ - K and Γ - M lines, consistent with the ARPES measurements [see Figs. 2(a), 2(b), and 2(d), and more discussions in the Supplemental Material [25]]. Meanwhile, the surface-localized states at the Sn surface are much reduced in their intensity compared to the Fe-Sn-1 surface (Fig. S7 in the Supplemental Material [25]) because the states originating from the Sn atoms are relatively weaker near E_F , as shown in Fig. S8 in the Supplemental Material [25]. Therefore, the Sn surface states are likely too weak to be visible in ARPES, and the flatband observed near E_F is originated mostly from the Fe-Sn-1 surface.

There are some weak fuzzy features below the observed flatband in the experimental ARPES result [Fig. 2(a)], which may originate from the strongly dispersive bands farther away from the surface, as shown in the calculated band structure of the Fe-Sn-1 surface structure [Fig. 2(c)].

Using STM, we also obtained differential conductance (dI/dV) spectra along the blue line on the Fe-Sn-1 surface [see Fig. 3(a)]. All the dI/dV spectra reflecting the LDOS show a prominent peak at ~ -0.2 V due to the flatband observed by ARPES. As shown in Fig. 3(b), the charge character of the flat-band state at ~ 0.2 eV below E_F represents quasilocized electrons originating from the Fe atoms, which encircle the hexagonal cells in the kagome lattice.

It is noteworthy that the ARPES spectra of Fe_3Sn_2 show not only the strong intensity around the Γ point at ~ 0.2 eV below E_F but also a limitation of the band flatness within a finite region of the Brillouin zone. This feature deviates from that obtained using a single-orbital tight-binding model for the ideal 2D kagome lattice, where a perfectly flatband extends over the whole Brillouin zone [5–7, 19]. Figure 3(b) shows the charge character of the flat-band state indicating a strong hybridization between the Fe-Sn-1 and Fe-Sn-2 layers. Physically, such an interlayer hybridization

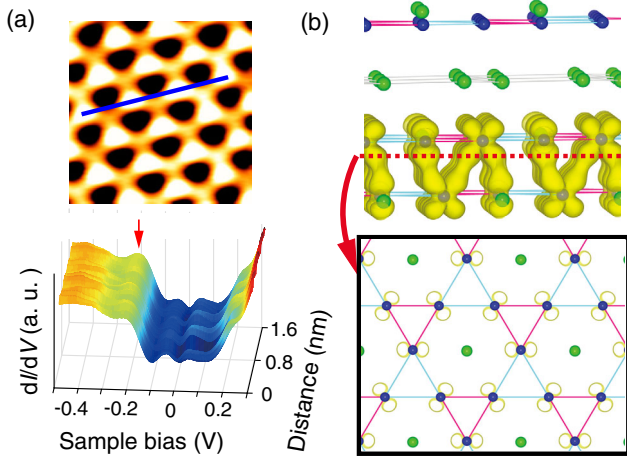


FIG. 3. Scanning tunneling spectroscopy of the Fe-Sn-1 surface. (a) Differential conductance (dI/dV spectra) scan (bottom) along the blue line on the STM image obtained at $V_s = -0.2$ V (top). (b) (Top) Calculated charge character of the flat-band state at the Γ point obtained from the Fe-Sn-1 surface structure. Here, the charge density distribution is drawn with an isosurface of $0.004 e/\text{bohr}^3$. (Bottom) A cross-section view drawn parallel to the Fe-Sn layers.

associated with the multi d orbitals of Fe atoms is likely to violate the precise destructive interference of Bloch electrons, leading to weakened band flatness observed in Fe_3Sn_2 . Based on these understandings, we develop a simple bilayer tight-binding model to explore the band evolution upon the strength of interlayer coupling (see details in the Supplemental Material [25]). As depicted in Fig. S9(a) of the Supplemental Material [25], the bilayer kagome lattice belongs to the point group D_{3d} containing the symmetry operations of a threefold rotation around the z axis, inversion, and mirror reflection with respect to the y - z plane. The calculated tight-binding band structures are shown in Figs. S9(b) and S9(c) of the Supplemental Material [25], which unambiguously demonstrate that the interlayer coupling weakens the band flatness.

Long-range ferromagnetic order has been previously observed in Fe_3Sn_2 [37–40]. Here, we also observed the ferromagnetic behaviors with a saturation magnetic moment of about $1.94 \mu_B$ per Fe atom at 2 K [Fig. 4(a)] and a Curie temperature T_c of ~ 610 K [Fig. 4(b)], consistent with previous experiments [37–39]. Moreover, we performed magnetic force microscopy measurements [41] (see more details in the Supplemental Material [25]), which is more sensitive to surface magnetization. A striped magnetic domain pattern is clearly seen in Figs. S10(b) and S10(c) of the Supplemental Material [25], further demonstrating the presence of long-range ferromagnetic order near the surface. It is noteworthy that the calculated surface band structure and simulated STM images of the nonmagnetic state of Fe_3Sn_2 (see Figs. S11 and S12 in the Supplemental Material [25]) substantially deviate from the experimental ARPES and STM results. Therefore, we

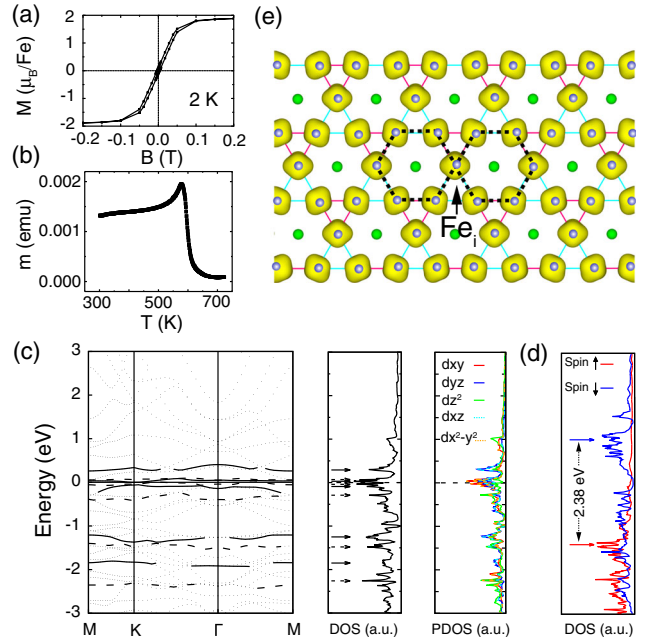


FIG. 4. Ferromagnetic order of Fe_3Sn_2 . (a),(b) Hysteresis loop (obtained at 2 K) and temperature-dependent magnetic moment (applied field of 100 Oe) of an Fe_3Sn_2 single crystal. Here, the magnetic field is applied parallel to the Fe-Sn layers. (c) Calculated band structure, DOS, and partial DOS for the nonmagnetic state of bulk Fe_3Sn_2 . The ten flatbands with dispersion smaller than 0.2 eV are drawn by solid or heavy dashed lines. (d) Calculated DOS for the ferromagnetic state of bulk Fe_3Sn_2 . (e) Spin density distribution of the ferromagnetic state. The spin density distribution is drawn with an isosurface of $0.01 e/\text{bohr}^3$.

can say that the presence of long-range ferromagnetic order is unambiguously validated even on the surface of Fe_3Sn_2 .

The mechanism of such a strong ferromagnetism in Fe_3Sn_2 , however, still remains open. Earlier theoretical studies reported that the extremely high degeneracy inherently associated with flatbands would naturally give rise to ferromagnetism when taking into account nonvanishing on-site Coulomb interaction [5–8]. In order to reveal the microscopic nature of the flat-band ferromagnetism in Fe_3Sn_2 , we calculated the band structure and partial DOS for the nonmagnetic bulk. We find that the DOS around the Fermi level mainly arise from the d orbitals of the Fe atoms [see Fig. 4(c)]. Here, the trigonal crystal field splits the five d orbitals into three categories, namely, d_{z^2} , $d_{xz,yz}$, and d_{xy,x^2-y^2} , the partial DOS of which are drawn in different colored lines. Since all the d orbitals participate in hopping within the present bilayer kagome lattice, we expect ten flatbands in bulk Fe_3Sn_2 , which can be identified from their narrow band dispersions and high DOS peaks [see Fig. 4(c)]. In particular, there are several nearly flatbands near E_F . Consequently, such high degenerate electronic states are mostly susceptible to the ferromagnetic order even with a tiny on-site Coulomb interaction [5–8]. The present DFT calculations indeed confirm that the

ferromagnetic configuration is more energetically stable than the nonmagnetic one by 2.18 eV per unit cell. Figure 4(d) displays the spin-polarized DOS showing a splitting of ~ 2.4 eV between the majority- and minority-spin bands [see Fig. S6(a) in the Supplemental Material [25]]. The calculated magnetic moment of $2.04 \mu_B/\text{Fe}$ for bulk Fe_3Sn_2 is close to the experimentally measured value of $1.94 \mu_B/\text{Fe}$ at 2 K [see Fig. 4(a)].

So far, we have shown that Fe_3Sn_2 has two remarkable aspects: i.e., flatbands of localized electrons and a long-range ferromagnetic ordering over the kagome lattice. Both aspects are attributed to the geometric character of the kagome lattice, which produces not only the destructive interferences of Bloch wave functions but also a mutually interconnecting network of hexagonal cells through the Fe atoms, i.e., Fe_i in Fig. 4(e). Thus, Fe_3Sn_2 can possess the local spin polarization due to the intramolecular exchange of localized electrons around each hexagon, and such spin moments are, in turn, coupled with each other via the intermolecular correlation. In the present system, we note that the Stoner parameter I is equivalent to the effective on-site Coulomb interaction U within the hexagonal cell [42]. For bulk Fe_3Sn_2 , I is roughly 1.15 eV estimated from dividing the exchange splitting by the magnetic moment [43,44]. It is noticeable that the Hubbard model on the kagome lattice has offered the two mechanisms for ferromagnetism: one is Mielke's flat-band ferromagnetism [5–7] that is an extreme case of the Stoner instability [45] reducing the potential energy of repulsive electron-electron interactions, and the other is Nakaoka-type ferromagnetism [46] due to the gain in the kinetic energy of electrons [47]. Interestingly, our DFT calculations demonstrate that the present system possesses the two aspects of ferromagnetism, including not only a large value of on-site U and the high DOS at the Fermi level caused by the self-trapping effect in kagome lattices but also the nearest-neighbor hopping due to the above-mentioned interconnecting lattice networks. Therefore, the observed high-temperature ferromagnetism would be attributed to the synergetic effects of the potential and kinetic energies in the kagome lattice, which is distinct from the itinerant ferromagnetism of other $3d$ transition metal compounds.

In summary, the present study has demonstrated for the first time the presence of flatbands in the realistic quasi-2D kagome compound of Fe_3Sn_2 , and further revealed that the flatbands attain the local spin polarization caused by an intramolecular exchange interaction as well as the long-range ferromagnetic order through a unique network of the hexagonal cells. This intriguing feature of flat-band ferromagnetism in the quasi-2D kagome lattice is quite distinctly contrasted with the recently observed ferromagnetism in 2D van der Waals crystals, where magnetic atoms are ferromagnetically coupled with the interelectronic exchange J [48,49]. Further control of the flat-band electronic structures, e.g., via charge doping, may enable realization of other versatile quantum phenomena [5–20].

This work was supported in part by the National Basic Research Program of China (Grant No. 2014CB921102), National Key Research and Development Program of China (Grants No. 2017YFA0403600 and No. 2017YFA0402903), National Natural Science Foundation of China (Grants No. 11434009, No. 11461161009, and No. 51627901), Anhui Initiative in Quantum Information Technologies, and Anhui Provincial Natural Science Foundation (Grant No. 1708085QA20). J.-H. C. is supported by the National Research Foundation of Korea grant funded by the Korea Government (Grants No. 2016K1A4A3914691 and No. 2015M3D1A1070639). S.Z. acknowledges the support by the U.S. Department of Energy under Grant No. DE-SC0002623. The calculations were performed by the KISTI supercomputing center through the strategic support program (Program No. KSC-2016-C3-0059) for supercomputing application research.

Z. L., J.-H. C., Q. Z., and W. Q. contributed equally to this work.

*Corresponding author.

cgzeng@ustc.edu.cn

†Corresponding author.

chojh@hanyang.ac.kr

- [1] W. A. Harrison, *Electronic Structure and the Properties of Solids: The Physics of the Chemical Bond* (Dover Publications, New York, 1989).
- [2] P. R. Wallace, The band theory of graphite, *Phys. Rev.* **71**, 622 (1947).
- [3] A. H. C. Neto, F. Guinea, N. M. R. Peres, K. S. Novoselov, and A. K. Geim, The electronic properties of graphene, *Rev. Mod. Phys.* **81**, 109 (2009).
- [4] S. Y. Zhou, G.-H. Gweon, J. Graf, A. V. Fedorov, C. D. Spataru, R. D. Diehl, Y. Kopelevich, D.-H. Lee, S. G. Louie, and A. Lanzara, First direct observation of Dirac fermions in graphite, *Nat. Phys.* **2**, 595 (2006).
- [5] A. Mielke, Ferromagnetic ground states for the Hubbard model on line graphs, *J. Phys. A* **24**, L73 (1991).
- [6] A. Mielke, Ferromagnetism in the Hubbard model on line graphs and further considerations, *J. Phys. A* **24**, 3311 (1991).
- [7] A. Mielke, Exact ground states for the Hubbard model on the Kagome lattice, *J. Phys. A* **25**, 4335 (1992).
- [8] H. Tasaki, Ferromagnetism in the Hubbard Models with Degenerate Single-Electron Ground States, *Phys. Rev. Lett.* **69**, 1608 (1992).
- [9] E. Tang, J.-W. Mei, and X.-G. Wen, High-Temperature Fractional Quantum Hall States, *Phys. Rev. Lett.* **106**, 236802 (2011).
- [10] K. Sun, Z. Gu, H. Katsura, and S. Das Sarma, Nearly Flatbands with Nontrivial Topology, *Phys. Rev. Lett.* **106**, 236803 (2011).
- [11] T. Neupert, L. Santos, C. Chamon, and C. Mudry, Fractional Quantum Hall States at Zero Magnetic Field, *Phys. Rev. Lett.* **106**, 236804 (2011).

- [12] Y.-F. Wang, Z.-C. Gu, C.-D. Gong, and D. N. Sheng, Fractional Quantum Hall Effect of Hard-Core Bosons in Topological Flat Bands, *Phys. Rev. Lett.* **107**, 146803 (2011).
- [13] C. Wu, D. Bergman, L. Balents, and S. Das Sarma, Flat Bands and Wigner Crystallization in the Honeycomb Optical Lattice, *Phys. Rev. Lett.* **99**, 070401 (2007).
- [14] S. D. Huber and E. Altman, Bose condensation in flat bands, *Phys. Rev. B* **82**, 184502 (2010).
- [15] M. Imada and M. Kohno, Superconductivity from Flat Dispersion Designed in Doped Mott Insulators, *Phys. Rev. Lett.* **84**, 143 (2000).
- [16] S. Peotta and P. Törmä, Superfluidity in topologically nontrivial flat bands, *Nat. Commun.* **6**, 8944 (2015).
- [17] Z. Liu, Z.-F. Wang, J.-W. Mei, Y.-S. Wu, and F. Liu, Flat Chern Band in a Two-Dimensional Organometallic Framework, *Phys. Rev. Lett.* **110**, 106804 (2013).
- [18] Y. Chen, Y. Y. Sun, H. Wang, D. West, Y. Xie, J. Zhong, V. Meunier, M. L. Cohen, and S. B. Zhang, Carbon Kagome Lattice and Orbital-Frustration-Induced Metal-Insulator Transition for Optoelectronics, *Phys. Rev. Lett.* **113**, 085501 (2014).
- [19] Z. Liu, F. Liu, and Y.-S. Wu, Exotic electronic states in the world of flat bands: From theory to material, *Chin. Phys. B* **23**, 077308 (2014).
- [20] J. Vidal, R. Mosseri, and B. Douçot, Aharonov-Bohm Cages in Two-Dimensional Structures, *Phys. Rev. Lett.* **81**, 5888 (1998).
- [21] D. Leykam, A. Andreanov, and S. Flach, Artificial flat band systems: From lattice models to experiments, *Adv. Phys.* **3**, 1473052 (2018).
- [22] S. Taie, H. Ozawa, T. Ichinose, T. Nishio, S. Nakajima, and Y. Takahashi, Coherent driving and freezing of bosonic matter wave in an optical Lieb lattice, *Sci. Adv.* **1**, e1500854 (2015).
- [23] R. Drost, T. Ojanen, A. Harju, and P. Liljeroth, Topological states in engineered atomic lattices, *Nat. Phys.* **13**, 668 (2017).
- [24] B. Malaman, B. Roques, A. Courtois, and J. Protas, Structure cristalline du stannure de fer Fe_3Sn_2 , *Acta Crystallogr. Sect. B* **32**, 1348 (1976).
- [25] See Supplemental Material at <http://link.aps.org/supplemental/10.1103/PhysRevLett.121.096401> for experimental and theoretical details as well as additional figures and discussions, which includes Refs. [26–32].
- [26] W. Kohn and L. J. Sham, Self-consistent equations including exchange and correlation effects, *Phys. Rev.* **140**, A1133 (1965).
- [27] P. E. Blöchl, Projector augmented-wave method, *Phys. Rev. B* **50**, 17953 (1994).
- [28] G. Kresse and D. Joubert, From ultrasoft pseudopotentials to the projector augmented-wave method, *Phys. Rev. B* **59**, 1758 (1999).
- [29] J. P. Perdew, K. Burke, and M. Ernzerhof, Generalized Gradient Approximation Made Simple, *Phys. Rev. Lett.* **77**, 3865 (1996).
- [30] G. Kresse and J. Furthmüller, Efficient iterative schemes for *ab initio* total-energy calculations using a plane-wave basis set, *Phys. Rev. B* **54**, 11169 (1996).
- [31] G. Kresse and J. Furthmüller, Efficiency of *ab initio* total energy calculations for metals and semiconductors using a plane-wave basis set, *Comput. Mater. Sci.* **6**, 15 (1996).
- [32] G. Makov and M. C. Payne, Periodic boundary conditions in *ab initio* calculations, *Phys. Rev. B* **51**, 4014 (1995).
- [33] C. J. Chen, *Introduction to Scanning Tunneling Microscopy* (Oxford University Press, New York, 1993).
- [34] Y. G. Ding, C. T. Chan, and K. M. Ho, Structure of the $(\sqrt{3} \times \sqrt{3})R30^\circ$ Ag/Si(111) Surface from First-Principles Calculations, *Phys. Rev. Lett.* **67**, 1454 (1991).
- [35] J. Tersoff and D. R. Hamann, Theory and Application for the Scanning Tunneling Microscope, *Phys. Rev. Lett.* **50**, 1998 (1983).
- [36] J. Tersoff and D. R. Hamann, Theory of the scanning tunneling microscope, *Phys. Rev. B* **31**, 805 (1985).
- [37] G. L. Caër, B. Malaman, and B. Roques, Mossbauer effect study of Fe_3Sn_2 , *J. Phys. F* **8**, 323 (1978).
- [38] B. Malaman, D. Fruchart, and G. L. Caër, Magnetic properties of Fe_3Sn_2 : II. Neutron diffraction study (and Mossbauer effect), *J. Phys. F* **8**, 2389 (1978).
- [39] L. A. Fenner, A. A. Dee, and A. S. Wills, Non-collinearity and spin frustration in the itinerant kagome ferromagnet Fe_3Sn_2 , *J. Phys. Condens. Matter* **21**, 452202 (2009).
- [40] L. Ye, M. Kang, J. Liu, F. von Cube, C. R. Wicker, T. Suzuki, C. Jozwiak, A. Bostwick, E. Rotenberg, D. C. Bell, L. Fu, R. Comin, and J. G. Checkelsky, Massive Dirac fermions in a ferromagnetic kagome metal, *Nature (London)* **555**, 638 (2018).
- [41] H. Zhou, Z. Wang, Y. Hou, and Q. Lu, A compact high field magnetic force microscope, *Ultramicroscopy* **147**, 133 (2014).
- [42] L. Severin, M. S. S. Brooks, and B. Johansson, Relationship between the Coulomb Integral U and the Stoner Parameter I , *Phys. Rev. Lett.* **71**, 3214 (1993).
- [43] J. D. Burton and E. Y. Tsymbal, Highly Spin-Polarized Conducting State at the Interface between Nonmagnetic Band Insulators: $\text{LaAlO}_3/\text{FeS}_2$ (001), *Phys. Rev. Lett.* **107**, 166601 (2011).
- [44] D. M. Edwards and M. I. Katsnelson, High-temperature ferromagnetism of sp electrons in narrow impurity bands: Application to CaB_6 , *J. Phys. Condens. Matter* **18**, 7209 (2006).
- [45] E. C. Stoner, Collective electron ferromagnetism, *Proc. R. Soc. A* **165**, 372 (1938).
- [46] Y. Nagaoka, Ferromagnetism in a narrow, almost half-filled s band, *Phys. Rev.* **147**, 392 (1966).
- [47] F. Pollmann, P. Fulde, and K. Shtengel, Kinetic Ferromagnetism on a Kagome Lattice, *Phys. Rev. Lett.* **100**, 136404 (2008).
- [48] C. Gong, L. Li, Z. Li, H. Ji, A. Stern, Y. Xia, T. Cao, W. Bao, C. Wang, Y. Wang, Z. Q. Qiu, R. J. Cava, S. G. Louie, J. Xia, and X. Zhang, Discovery of intrinsic ferromagnetism in two-dimensional van der Waals crystals, *Nature (London)* **546**, 265 (2017).
- [49] B. Huang, G. Clark, E. Navarro-Moratalla, D. R. Klein, R. Cheng, K. L. Seyler, D. Zhong, E. Schmidgall, M. A. McGuire, D. H. Cobden, W. Yao, D. Xiao, P. Jarillo-Herrero, and X. Xu, Layer-dependent ferromagnetism in a van der Waals crystal down to the monolayer limit, *Nature (London)* **546**, 270 (2017).